Check for updates

ADVANCED FUNCTIONAL MATERIALS
www.afm-journal.de

Carrier Trapping Deactivation by Halide Alloying in Formamidinium-Based Lead Iodide Perovskites

*Jesús Jiménez-López, Daniele Cortecchia, E. Laine Wong, Giulia Folpini, Antonella Treglia, Ada Lilí Alvarado-Leaños, Chun-Sheng Wu, Andrea Olivati, and Annamaria Petrozza**

Formamidinium lead iodide ($FAPbI_3$) is the benchmark material for the most efficient near-infrared perovskite light-emitting diodes (LEDs) and a promising gain medium for perovskite-based coherent light sources. Thus, it is crucial to understand and control its defect chemistry to harness the full potential of its exceptional radiative recombination properties. Here, this topic is addressed by tailoring the I^- to Br^- ratio in the perovskite composition. It is found that introducing small Br^- quantities improves the yield of radiative recombination with a beneficial impact on both spontaneous and amplified spontaneous emission (ASE) and improves the semiconductor photostability leading to reduced luminescence efficiency roll-off and enhanced radiance in LEDs. By employing photoemission electron microscopy (PEEM), this improvement in optoelectronic performance can be directly correlated to a reduced hole-trapping activity achieved by replacing iodide with bromide, thus, providing a convenient yet powerful synthetic approach to control the defect chemistry of the material and fostering its implementation in advanced photonic platforms.

1. Introduction

Outstanding optoelectronic properties and cost-effective fabrication procedures have put metal halide perovskites in the spotlight to become the next photovoltaic and photonic technology on the market. Among the different chemical compositions, formamidinium lead iodide ($FAPbI_3$) offers the highest photovoltaic efficiency[1] and is the current state-of-the-art composition for near-infrared emitters.[2] The high radiative recombination yield and record performance in LEDs[2b,c] make it appealing also for coherent emission and an excellent candidate for the realization of the long sought-after perovskite-based electrically pumped lasers.[3] Despite its many advantages, the investigation into $FAPbI_3$-based laser has lagged behind other perovskite candidates, such as $MAPbI_3$[4] and multidimensional perovskites[5] due to its phase instability[6] in ambient conditions. For the development of LEDs, a typical synthetic approach to overcome phase instability involves the use of a large excess of FA^+ to promote the formation and stabilization of the black α-phase.[2a,d] Furthermore, the excess FA^+ has been reported to passivate deep trap states at the grain boundaries.[7] It is possible that these particularities in the synthetic conditions of perovskites may lead to differences in the defect chemistry of these materials. Interstitial iodide, which introduces electron and hole deep traps,[8] has been recently recognized as a point defect strongly influencing lead halide perovskite semiconductors. While the electron traps are long-lived and inactive upon steady–state excitation, the short-lived hole traps are detrimental species affecting the device performance of iodide-based lead perovskites.[8a,b] Partial substitution of I^- with Br^- has often been noticed to improve the radiative emission of the semiconductors with varying outcomes. Some works reported the formation of micrometer-sized Br^- rich domains giving rise to energy funneling mechanism, promoting radiative recombination processes.[9] Nonradiative carrier recombination might be further reduced due to the partial inhibition of FA^+ rotational modes associated with a preferred orientation of FA^+ toward the Br^- anions in the unit cell that are able to form stronger hydrogen bonds compared to I^-.[10] Nevertheless, direct evidence of these effects has remained elusive and the practical implications for the material and device performance are not well understood.

In this work, we study the effect of Br^- addition on the defectivity of $FAPbI_3$ and its impact on photonic applications. We find that Br^- is incorporated in the crystal structure of the host $FAPbI_3$ without evident phase segregation. Br^- nominal concentrations

J. Jiménez-López, D. Cortecchia, E. L. Wong, G. Folpini, A. Treglia, A. L. Alvarado-Leaños, C.-S. Wu, A. Olivati, A. Petrozza
Center for Nano Science and Technology
Istituto Italiano di Tecnologia
Milan 20134, Italy
E-mail: annamaria.petrozza@iit.it

D. Cortecchia
Dipartimento di Chimica Industriale "Toso Montanari"
Università di Bologna
Bologna 40129, Italy

A. Treglia, A. L. Alvarado-Leaños, C.-S. Wu, A. Olivati
Physics Department
Politecnico di Milano
Milan 20133, Italy

The ORCID identification number(s) for the author(s) of this article can be found under https://doi.org/10.1002/adfm.202308545

© 2023 The Authors. Advanced Functional Materials published by Wiley-VCH GmbH. This is an open access article under the terms of the Creative Commons Attribution-NonCommercial License, which permits use, distribution and reproduction in any medium, provided the original work is properly cited and is not used for commercial purposes.

DOI: 10.1002/adfm.202308545

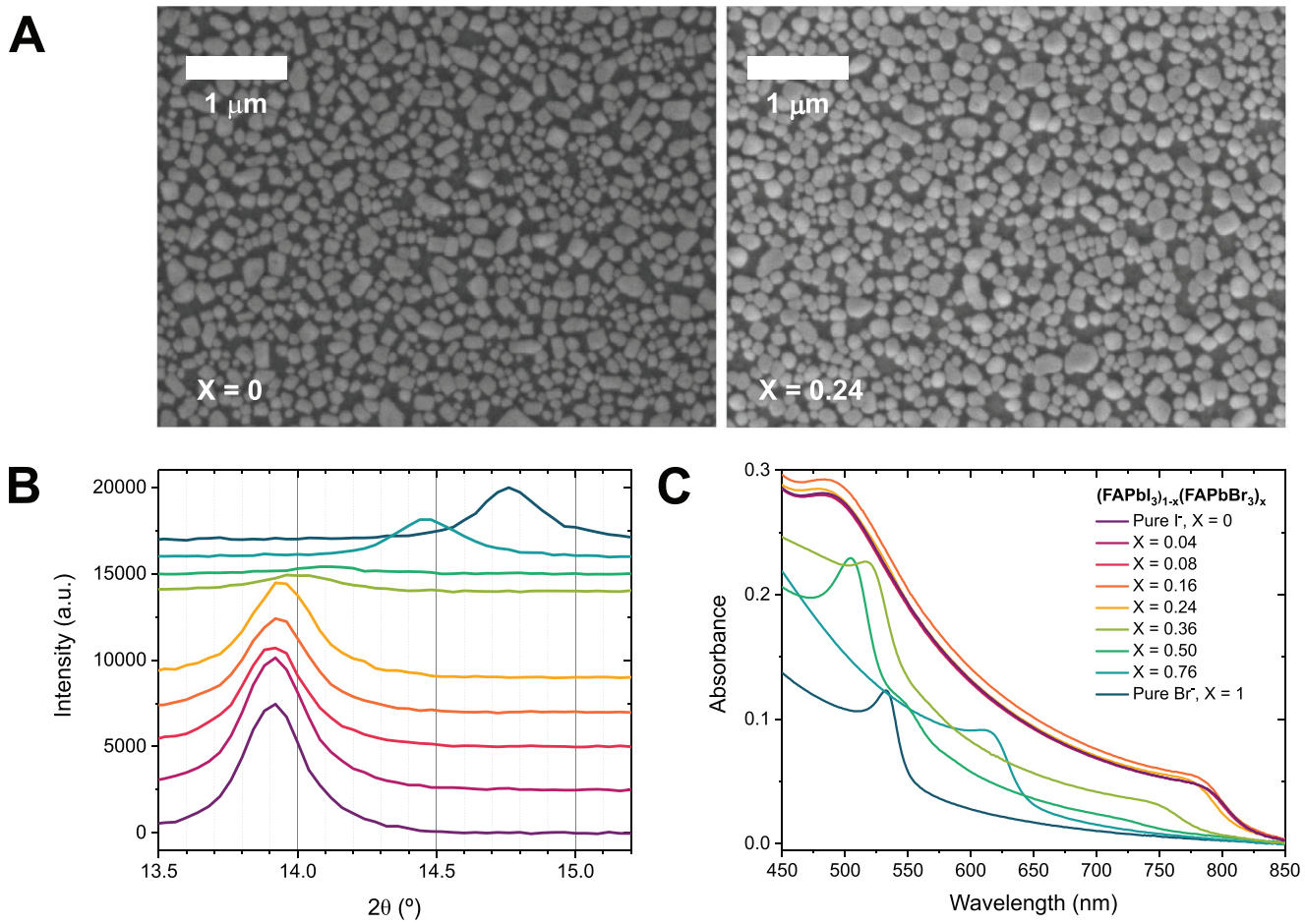

Figure 1. A) Top view SEM images of $(FAPbI_3)_{1-x}(FAPbBr_3)_x$ with $X = 0$ (left) and $X = 0.24$ (right). Scale bar is 1 μm. B) XRD patterns for the different $(FAPbI_3)_{1-x}(FAPbBr_3)_x$ compositions. C) UV–vis absorption spectra for the different $(FAPbI_3)_{1-x}(FAPbBr_3)_x$ compositions.

in the range $X = 0.08$–0.24 lead to spectrally stable perovskite compositions, with an enhancement of the radiative recombination efficiency, higher photoluminescence quantum yield, increased brightness, and reduced roll-off in LEDs. In turn, optical gain is also positively affected in formulations with optimal Br^-/I^- ratio, yielding a lower threshold of optically pumped ASE, which remains stable under applied bias. Photoemission electron microscopy reveals that the incorporation of a small nominal amount of Br^- during the thin film growth photostabilizes the perovskite by affecting the activity of those defects responsible for carrier trapping and material degradation.[8b] Our findings highlight the key role of bromide addition providing an effective defect-engineering strategy to improve the optoelectronic quality of $FAPbI_3$ and further enhance its performance for photonic applications.

2. Results and Discussion

2.1. Bromide Incorporation into Formamidinium Lead Iodide Perovskite

We fabricated formamidinium-based lead halide perovskite films with high crystalline and optoelectronic quality. The synthesis of these perovskite films is based on previous reports in which the use of large formamidinium (FA^+) cation excess in combination with the use of 5-aminovaleric acid iodide (5-AVAI) as an additive is used to promote the formation of isolated perovskite domains with cubic α perovskite phase.[2a] We mixed different ratios of pure iodide formamidinium perovskite ($FAPbI_3$) in combination with pure bromide formamidinium perovskite ($FAPbBr_3$) to give the final mixed-halide formamidinium perovskite compositions $[(FAPbI_3)_{1-x}(FAPbBr_3)_x$, where $x = 0$, 0.04, 0.08, 0.16, 0.24, 0.36, 0.5, 0.76, 1].

All the $(FAPbI_3)_{1-x}(FAPbBr_3)_x$ films present similar morphologies (Figure S1, Supporting Information). As expected, with this synthetic approach, we observed the formation of faceted nanoplatelets[2a] with a similar distribution of sizes from 90 to 250 nm independent of the halide composition (**Figure 1A**; Figure S1, Supporting Information). The XRD patterns show that all the perovskite compositions except for $X = 0.36$ and $X = 0.5$ present XRD peaks of high crystallinity, characteristic of the cubic α crystallographic phase (Figure 1B; Figure S2, Supporting Information). For $FAPbI_3$, these peaks are located at 13.9° and 28° corresponding to the (001) and (002) crystallographic planes, shifting to 14.8° and 29.8°, respectively, for $FAPbBr_3$ due to the lattice contraction associated with the smaller size of the Br^- anion. The

© 2023 The Authors. Advanced Functional Materials published by Wiley-VCH GmbH

16163028, 0, Downloaded from https://onlinelibrary.wiley.com/doi/10.1002/adfm.202308545 by Area Sistemi Dipart & Document, Wiley Online Library on [22/01/2024]. See the Terms and Conditions (https://onlinelibrary.wiley.com/terms-and-conditions) on Wiley Online Library for rules of use; OA articles are governed by the applicable Creative Commons License

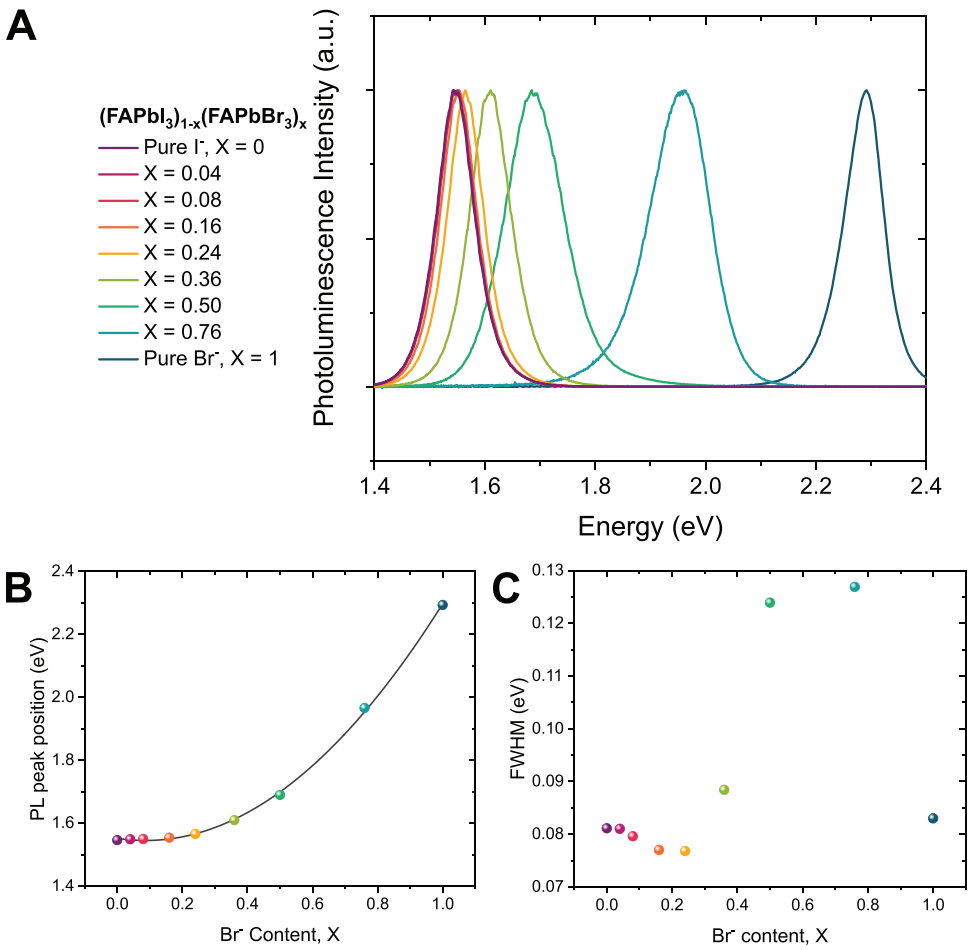

Figure 2. A) Photoluminescence spectra of $(FAPbI_3)_{1-x}(FAPbBr_3)_x$ samples measured under 450 nm excitation. B) Photoluminescence peak position, and C) full-width at half maximum of the photoluminescence spectra obtained from the fitting of the PL spectra in (A). The line in (B) is the fit to Vegard's law expression.

very low crystallinity of $X = 0.36$ and $X = 0.5$ is correlated with the phase instability within these halide ratios in pure FA^+ halide perovskites, in agreement with previous reports.[11] Only the α black phase (XRD peaks between $2\theta = 14°$ and 15° depending on the perovskite composition, Figure S2, Supporting Information) with no characteristic XRD peaks associated with the detrimental δ yellow phase is obtained using this synthetic procedure, even with the use of low annealing temperatures (100 °C). The smaller than expected shift in the (001) XRD peak (Figure 1B) based on the nominal stoichiometric composition suggests that not all the bromide in the precursor solutions is incorporated into the perovskite lattice. Following the FWHM of the (001) XRD peak, it slightly broadens with the increase in Br^- content up to $X = 0.24$ (FWHM ($X = 0$)= 0.29; FWHM ($X = 0.24$)= 0.31). Given the similar grain sizes, we assigned this peak broadening to chemical heterogeneity,[12] which also confirms the Br^- incorporation into the crystal structure.

The UV–vis absorption spectra of the samples with $x \leq 0.24$ (Figure 1C) resemble the spectra of pure iodide $FAPbI_3$, with a sharp absorption edge located at ≈800 nm.[11,13] However, the band edge starts shifting to higher energies, associated with an enlarged bandgap due to the incorporation of Br^- in the lattice (Figure S3, Supporting Information). This shift is very small for perovskite compositions below $X = 0.16$ and starts to be more noticeable for $X = 0.24$. Consistent with our XRD analysis, samples $X = 0.36$ and $X = 0.5$ show less sharp absorption onsets, which will indicate higher Urbach energies (E_U), characteristic of samples with a high structural disorder and low crystallinity.[14] Pure bromide samples, $X = 1$, as expected, present excitonic properties, characteristic of this material system, associated with the higher exciton binding energy of bromide perovskites compared to the iodide counterparts.[15]

The photoluminescence (PL) spectra of these samples (**Figure 2A**; Figure S4A, Supporting Information, for the nonnormalized PL spectra) show a shift of the PL peaks toward higher energies (Figure 2B; Figure S4B, Supporting Information) as a function of the Br^- ratio, from 1.54 eV for $X = 0$, $FAPbI_3$, to 2.29 eV for $X = 1$, $FAPbBr_3$. This PL shift follows Vegard's law[16] (Note S1, Supporting Information). We obtained a bowing parameter, $b = 0.9$. However, one would expect smaller deviations from the linearity of the PL peak with the Br^- content[13a,16,17] (Figure 2B). This is not our case, especially in compositions close to $X = 0$, confirming that only a small fraction of Br^- in the perovskite precursor solution is effectively incorporated into the perovskite lattice.

© 2023 The Authors. Advanced Functional Materials published by Wiley-VCH GmbH

16163028, 0, Downloaded from https://onlinelibrary.wiley.com/doi/10.1002/adfm.202308545 by Area Sistemi Dipart & Document, Wiley Online Library on [22/01/2024]. See the Terms and Conditions (https://onlinelibrary.wiley.com/terms-and-conditions) on Wiley Online Library for rules of use; OA articles are governed by the applicable Creative Commons License

Similar trends are observed if the perovskite synthesis is done with $PbBr_2$ as the only source of Br^-, avoiding the large excess of FABr added in the perovskite precursor (Figure S5, Supporting Information). Several possible explanations for this behavior can be found in the literature. Long et al.[18] found out that in triple cation perovskite compositions, FABr evaporates during the annealing step, even with mild annealing temperatures. Meggiolaro et al.[8a] suggested that Br^- could substitute two different I^- positions in pure iodide perovskite, either an interstitial iodide or a lattice iodide. They calculated that Br^- will preferentially substitute interstitial I^- first instead of lattice I^-. Another explanation is the one suggested by Diez-Cabanes et al.,[19] where they observed that the PL peak shifts in energy in mixed-halide perovskite films with an apparently homogeneous emission, due to the formation of spatially separated halide phases on a nanometric scale.

The full width at half maximum (FWHM) obtained from the PL spectrum can be directly correlated with the Urbach energy,[14b,20] allowing for a reliable comparison of the phase stability and structural order. The FWHM shows similar values from $X = 0$ to $X = 0.24$, indicating that the small addition of Br^- into the perovskite lattice results in phase-stable perovskite of higher structural order. This is further confirmed with photothermal deflection spectroscopy (PDS) measurements.[14a] The Urbach energies (E_U) are obtained from the fitting of the absorption onset of the PDS measurements, allowing a direct correlation with the degree of disorder of the semiconductor.[14a] We obtained very similar Urbach energies (Figure S6, Supporting Information, E_U values between 37 and 38 meV for all the perovskite compositions), confirming that phase stable perovskites are obtained for compositions ranging $X = 0$–0.24, despite adding Br^- to the perovskite structure. Higher Br^- concentrations ($X > 0.24$) result in higher values of FWHM, as expected, from the low stability that we have previously described. In addition to that, we also observe that the incorporation of Br^- into the perovskite lattice forms a single phase homogeneously distributed throughout the film, without the formation of micrometer-sized domains where carriers might funnel from the Br-rich to the I-rich domains.[9] Using PL mapping (Figure S7, Supporting Information), we observe a homogeneous emission in a micrometer scale in all the film, which blueshifts with higher Br^- contents. In addition, for perovskite compositions $X \leq 0.24$ the introduction of Br^- does not result in spectral instabilities (Figures S8 and S9, Supporting Information), as it is to be expected in mixed halide compositions due to halide segregation upon photoexcitation of the samples, creating I-rich and Br-rich phases in the film.[21] The stability of these samples is explained due to the use of excess FA^+ salts, which passivate defects at the grain boundaries,[7] suppressing halide migration, as previously suggested by Zhou et al.[22]

After a careful analysis of the structural and optical properties with different Br^- ratios, we can conclude that the incorporation of small nominal Br^- quantities, up to $X \leq 0.24$, results in FA-based perovskite films showing one single phase of high optical and crystalline quality.

2.2. Bromide Effects on Emissive Properties

After having identified the optimal Br^- ratios to minimize the structural disorder, we explore how Br^- affects the emissive properties at different carrier injection regimes focusing on the most stable compositions with the highest optical quality $X = 0$, 0.08, 0.16, and 0.24 (**Figure 3A,B**). At low excitation densities, where trap-assisted recombination is predominant, the inclusion of small Br^- quantities ($X = 0.16$ and 0.24) leads to higher PLQY associated with a reduced carrier trap activity. Additionally, we measured the absolute values of PLQY at an excitation density of 10^{15} cm^{-3} (Figure 3B), where trap-assisted nonradiative recombination still dominates.[23] PLQY values increase from 20.7% for $X = 0$ to 28.4% for $X = 0.16$. Therefore, incorporation of Br^- into $FAPbI_3$ results in an improved radiative recombination via a reduction of the trap-induced nonradiative recombination. At higher excitation density ($>10^{18}$ cm^{-3}) Auger–Meitner recombination becomes the predominant mechanism,[23a] resulting in similar PLQY for all the samples (Figure 3A).

We also explored the gain characteristics of these materials. For this purpose, we checked their ASE performance (Figure 3C–F). Fluence dependence measurements of materials showing ASE are described by two different regimes (Figure 3E), a linear increase of the PL with the fluence followed by a superlinear increase once ASE dominates together with the narrowing of the emission bandwidth (Figure 3F). Figure 3C,D compares the best ($X = 0.24$) and worst ($X = 0.08$) ASE-performing samples. All the ASE spectra are shown in Figure S10 (Supporting Information). We observe a reduction of the ASE thresholds from 15.8 μJ cm^{-2} for $FAPbI_3$ to 12.3 and 12.5 μJ cm^{-2} for the samples with $X = 0.16$ and 0.24, respectively. A higher threshold of 18.6 μJ cm^{-2} was found for $X = 0.08$. Apart from the lower thresholds, we also observe a steeper slope in the case of $X = 0.16$ and 0.24, and, at every laser fluence, higher ASE intensities for $X = 0.16$ and $X = 0.24$ (Figure S11, Supporting Information). The fitted FWHM of the PL peaks shows the expected spectral narrowing characteristic of ASE (Figure 3F). All the samples present similar spectral narrowing from 50 to ≈7 nm over the broader PL spectrum.

Overall, the introduction of Br^- results in better emissive properties of the material. However, the best performances require a minimum Br^- content for this passivation to take place, which starts to be observable at $X = 0.16$.

2.3. Bromide Incorporation Effects on Perovskite Light-Emitting Diodes (PeLEDs)

We fabricated PeLEDs with the following architecture (**Figure 4A**; Figure S12, Supporting Information, for the cross-section) ITO/ZnO:PEIE/$(FAPbI_3)_{1-x}(FAPbBr_3)_x$/TFB/$MoO_3$/Au, where ZnO nanoparticles modified with a thin layer of PEIE to modify the work function and to reduce the chemical activity of ZnO is employed as the n-type injection layer and TFB is employed as the p-type injection layer. A large excess of FA^+ was employed (2.45:1, FA^+:Pb^{2+}, molar ratio) to promote the crystallization of the α-$FAPbI_3$ perovskite phase,[2a,24] and to passivate traps at the surface of the perovskite grains.[7] We also employed 5-AVAI or 5-AVABr that reacts with the basic ZnO, following a deprotonation reaction leading to the formation of a very thin insulating layer at the ZnO/perovskite interface,[2a] inhibiting the ZnO activity[2a,25] responsible for the degradation of the perovskite grains.

© 2023 The Authors. Advanced Functional Materials published by Wiley-VCH GmbH

16163028, 0, Downloaded from https://onlinelibrary.wiley.com/doi/10.1002/adfm.202308545 by Area Sistemi Dipart & Document, Wiley Online Library on [22/01/2024]. See the Terms and Conditions (https://onlinelibrary.wiley.com/terms-and-conditions) on Wiley Online Library for rules of use; OA articles are governed by the applicable Creative Commons License

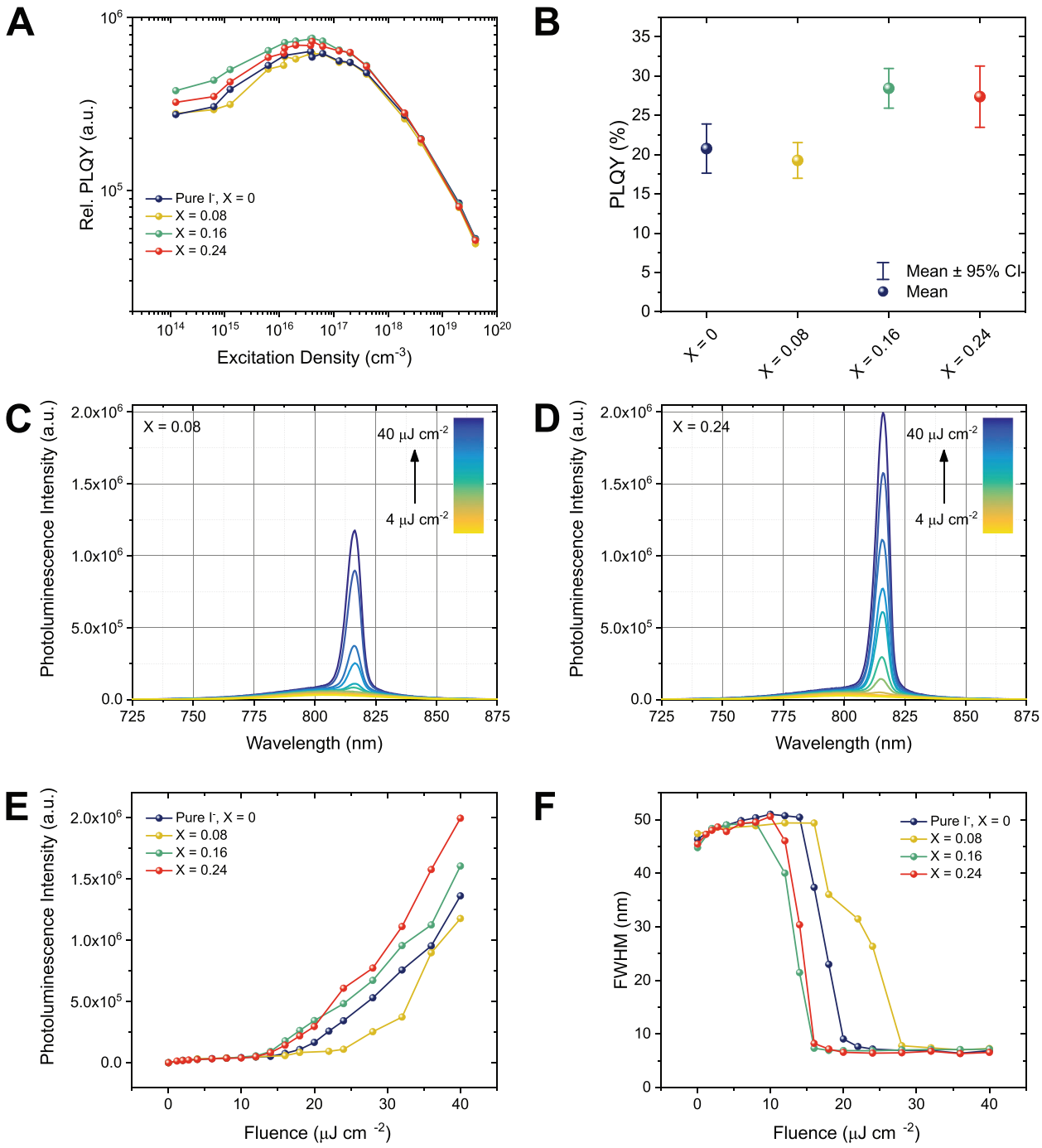

Figure 3. A) Relative PLQY as a function of excitation density for the targeted samples, $X = 0$, $X = 0.08$, $X = 0.16$, and $X = 0.24$, measured under a 515 nm excitation laser pulse at a 500 kHz repetition rate. B) Absolute PLQY values obtained with a 560 nm CW laser at an excitation density of 10^{15} cm^{-3}. C,D) Fluence-dependent PL of $x = 0.08$ and $X = 0.24$ measured under 532 nm excitation laser pulse and 1 kHz repetition rate. E) Peak intensity, and F) FWHM as a function of the excitation fluence.

Perovskite LED electroluminescence behaves similarly to the observed PL. A sharp and narrow electroluminescence peak is observed at 804 nm for $FAPbI_3$ ($X = 0$), showing a progressive blue-shift with the insertion of Br^- (Figure 4B) that once again is lower than expected for high iodide concentration values based on the nominal stoichiometric compositions. Also, it should be noted that the electroluminescence spectra peak position of $X = 0.24$ remained stable independently of the applied voltage (Figure S13, Supporting Information). Next, we analyzed the LEDs EQE characteristics, highlighting the reduced roll-off with the increased Br^- concentration in the perovskite composition (Figure 4C). Roll-off is used in LEDs to describe

© 2023 The Authors. Advanced Functional Materials published by Wiley-VCH GmbH

16163028, 0, Downloaded from https://onlinelibrary.wiley.com/doi/10.1002/adfm.202308545 by Area Sistemi Dipart & Document, Wiley Online Library on [22/01/2024]. See the Terms and Conditions (https://onlinelibrary.wiley.com/terms-and-conditions) on Wiley Online Library for rules of use; OA articles are governed by the applicable Creative Commons License

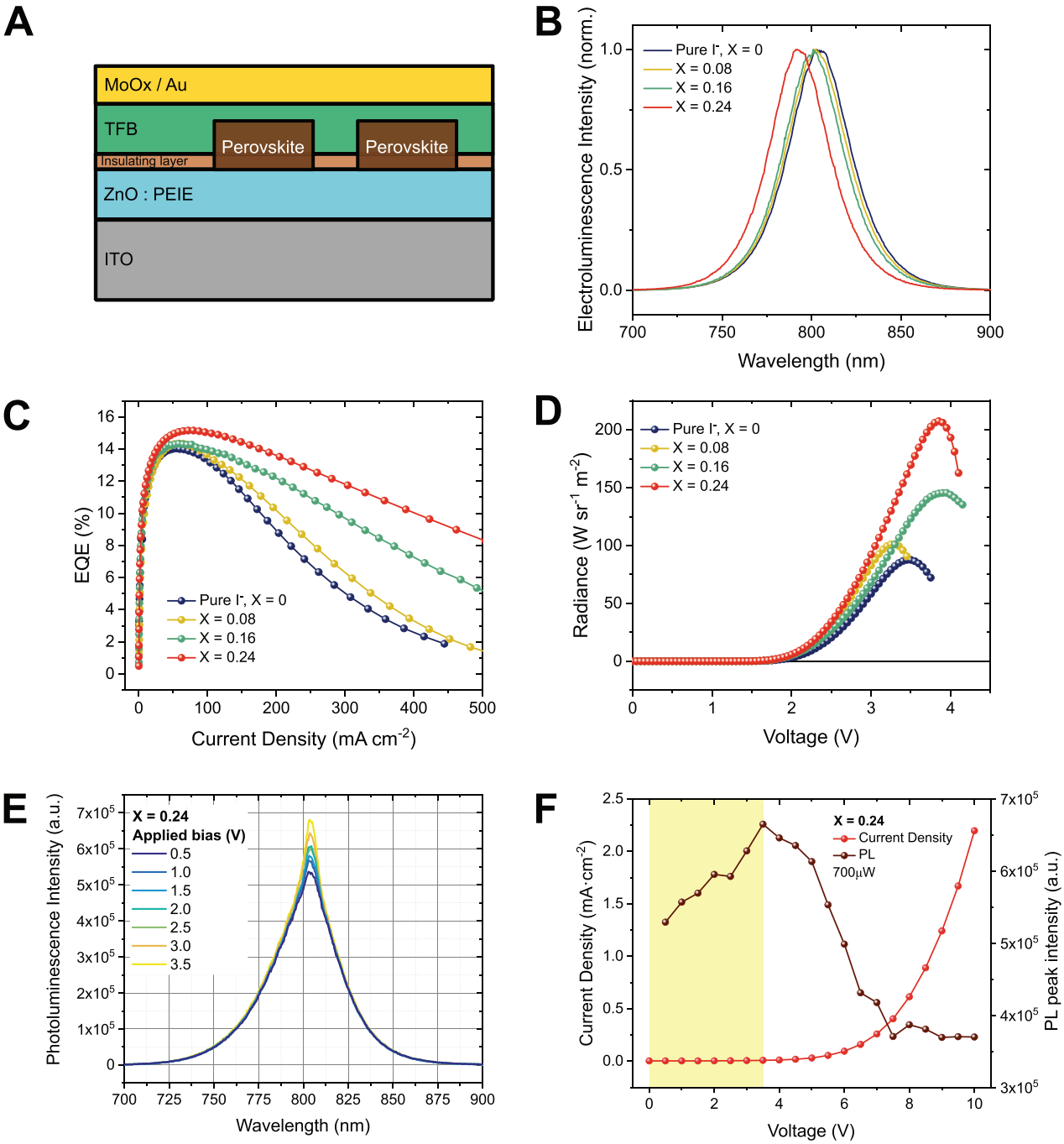

Figure 4. A) Scheme showing the employed PeLED architecture. B) Normalized electroluminescence spectra obtained at 2.5 V. C) External quantum efficiency as a function of the current density. D) Radiance as a function of the applied voltage. E) Photoluminescence spectra of $X = 0.24$ using an LED architecture acquired with an applied positive bias $V = 0$–3.5 V and using a 532 nm laser pulse as the excitation source. F) Current density and registered PL peak intensity of $X = 0.24$ as a function of applied bias. The PL values are taken from the maximum emission at 804 nm. The highlighted area is the voltage range shown in Figure 4E.

the efficiency losses when higher current densities are applied to the device.[3a,26] For perovskites, roll-off has been assigned to increased Auger–Meitner recombination,[27] charge carrier injection imbalance,[28] electric field induced quenching,[27b] or Joule heating.[27a,29] Recent studies have also demonstrated the correlation between ion migration and roll-off in devices.[30] Not only we observe better performances correlated to reduced roll-off, but we also reported higher efficiencies compared to pure I^- samples (15.1% for $X = 0.24$ and 14.0% for $X = 0$). The maximum radiance values, obtained in every case at higher current densities, also increase with the increasing Br^- content, and corresponding roll-off reduction, (Figure 4D; Figure S14, Supporting

© 2023 The Authors. Advanced Functional Materials published by Wiley-VCH GmbH

16163028, 0, Downloaded from https://onlinelibrary.wiley.com/doi/10.1002/adfm.202308545 by Area Sistemi Dipart & Document, Wiley Online Library on [22/01/2024]. See the Terms and Conditions (https://onlinelibrary.wiley.com/terms-and-conditions) on Wiley Online Library for rules of use; OA articles are governed by the applicable Creative Commons License

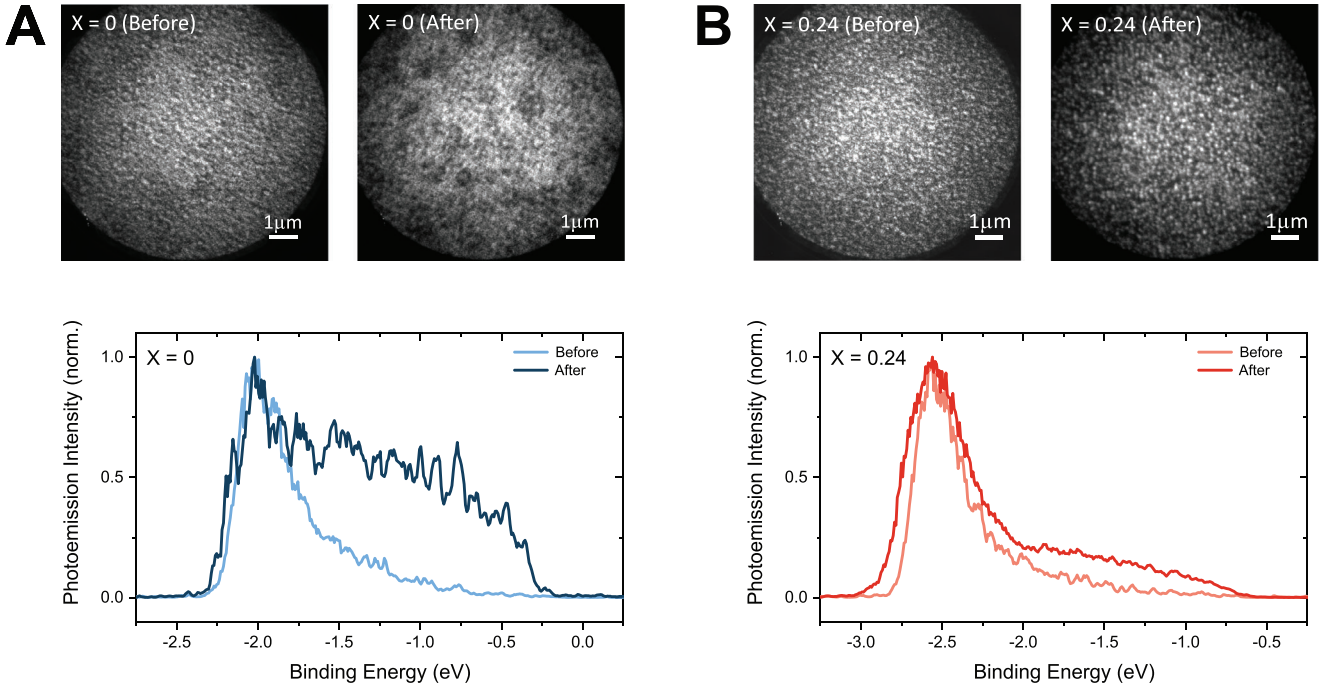

Figure 5. A) Spatially integrated PEEM image of $X = 0$, before (top left) and after (top right) light soaking. Normalized photoemission spectra (bottom) obtained from the images shown above. B) Spatially integrated PEEM image of $X = 0.24$, before (top left) and after (top right) light soaking. Normalized photoemission spectra (bottom) obtained from the images shown above.

Information), from 87 W sr^{-1} m^{-2} for $FAPbI_3$ ($X = 0$), to 101, 145, and 207 W sr^{-1} m^{-2} for $X = 0.08$, 0.16, and 0.24, respectively.

The identification of low-defectivity compositions with low ASE threshold and reduced roll-off in LEDs allowed us to further investigate the gain characteristics of the material under electrical bias in a full-device configuration,[31] (Figure S15A, Supporting Information) which is of high relevance toward the development of electrically pumped lasers. Here, we selected $X = 0.24$, which gives the best results in terms of device efficiency and roll-off, and further optimized the device to improve the light confinement into the perovskite layer and reduce optical losses at the metal electrode[32] by increasing the thickness of the TFB layer (see the full details in Experimental Section). Even though this affects the charge transport, leading to J–V curves with lower currents (Figure S15B, Supporting Information), we found it to be a necessary step to preserve the optical gain properties. In Figure S15C (Supporting Information), we show the optically pumped ASE on complete devices, with persisting and stable ASE observed over periods of more than 20 min (Figure S15D, Supporting Information). Upon application of a positive bias in the range 0–3.5 V (Figure 4E), both luminescence and ASE are enhanced. In this range, the contribution of electroluminescence to the luminescence signal is negligible (Figure S15E,F, Supporting Information); however, when the exponential part of the J–V curve starts to be prominent, meaning that charges are flowing into the device, the EL starts to be observable and concurrently the ASE decreases in intensity (Figure 4F; Figure S16, Supporting Information). In agreement with previous reports,[31a,33] we correlate the improved ASE performance in the voltage range 0–3.5 V with the redistribution of mobile ions: under bias, the negative and positive ions are dragged from the hole and electron transport layer interfaces, respectively, where they accumulate creating regions of increased nonradiative recombination. Ions redistribute in the bulk of the perovskite, and therefore, radiative recombination is promoted.[33] The effect of ionic redistribution further stresses the crucial need to control the defect density in order to enhance the recombination properties and improve the gain characteristics of the perovskite.

2.4. Bromide Influence on Defect Activity

We investigated the mechanism behind the improvement in optoelectronic properties with halide alloying in FA-based perovskites. First, we measured the photoemission spectra of the samples containing $X = 0$ and $X = 0.24$ (**Figure 5**; Figures S17 and S18, Supporting Information) with a photoemission electron microscope (PEEM). Using PEEM it is possible to space-resolve the energetic positions of the valence band and the intragap states, making it a useful technique to study defects and their associated energetic levels in perovskite and correlate it to the morphological characteristics of the sample.[34]

Figure 5 shows the spatially integrated PEEM images, which give an estimate of the total number of photoemitted electrons in the area of interest, before and after light soaking, i.e., after long periods of light illumination (Figures S16 and S17, Supporting Information). First, it is possible to observe that $X = 0.24$ has a much better photostability compared to pure I^-, $X = 0$ samples (Figure 5). In both samples, at the beginning of the experiment, a single photoemission peak is detected, correlated to the valence band position. The second feature, previously associated with deep hole traps by Stranks and co-workers,[34]

© 2023 The Authors. Advanced Functional Materials published by Wiley-VCH GmbH

16163028, 0, Downloaded from https://onlinelibrary.wiley.com/doi/10.1002/adfm.202308545 by Area Sistemi Dipart & Document, Wiley Online Library on [22/01/2024]. See the Terms and Conditions (https://onlinelibrary.wiley.com/terms-and-conditions) on Wiley Online Library for rules of use; OA articles are governed by the applicable Creative Commons License

becomes visible only after light soaking, and it is much more intense for $X = 0$. After light soaking, we observed the formation of dark areas (Figure 5) associated with a higher defect density and film degradation (Figure S17, Supporting Information) in $X = 0$, which are not present in $X = 0.24$. The incorporation of Br^- results in more homogeneous photoemission, which is related to the improved photostability of the material.

In Figures S16 and S17 (Supporting Information), we show the spatially resolved PEEM images, which have been referenced to Au markers to determine their respective binding energies.[34] The introduction of Br^- results in two different effects. First, the work function is reduced. Second, the intensity of the feature associated with hole traps is lower in intensity in the Br^- containing sample, $X = 0.24$, compared to the pure I^-, $X = 0$, sample (Figures S17 and S18, Supporting Information). Furthermore, the onset of the trap-associated energetic levels is shifted to higher binding energies, ≈0.3 eV in $X = 0.24$ (Figure S18, Supporting Information). This value, 0.3 eV, was pointed out to be the energy difference between the deep hole trap levels associated with interstitial I^- and the shallower hole trap levels from the interstitial Br^-, which would be the reason behind the deactivation of such trap states.[8a] However, we do not observe this shift in energy when $X = 0.08$ (Figure S18, Supporting Information). This indicates that higher Br^- concentrations are required to deactivate the deep trap states associated with interstitial iodide. Using PEEM, we have direct evidence of the reduced trap activity and the deactivation of specific trap levels after halide alloying, resulting in photostable materials with improved optoelectronic properties.

To further confirm the healing effect over the deep hole traps with the small addition of Br^-, we performed time-resolved photoluminescence (TRPL) and observed longer PL lifetimes in Br-containing samples (Figures S19 and S20, Supporting Information). We perform these measurements at excitation densities below trap filling (10^{15} cm^{-3}), as shown by the monoexponential PL decay associated with dominant trap-assisted recombination (Figure S20, Supporting Information). The longer PL lifetime for $X = 0.08$ and $X = 0.24$ (2.4 µs compared to 1.6 µs for $X = 0$) stands to show the reduced defect activity upon Br^- addition.

We suggest the following mechanism to explain the improved photostability of the material. Interstitial iodide introduces two types of deep defect levels, long-lived electron traps and short-lived hole traps. While the long-lived electron traps are inactive, the short-lived hole traps are detrimental, leading to increased nonradiative recombination.[8a,b] Apart from that, the carrier capture at the interstitial iodide positions leads to the formation of the neutral interstitial iodide species (I_i^0), which will react to form I_2. Then, I_2 will be expelled from the film, leading to photodegradation in the perovskite film.[35] When small amounts of Br^- are added to pure I^- perovskite compositions, Br^- tends to substitute the interstitial iodide positions before reaching the lattice iodide positions.[8a] The substitution of iodide with bromide at the interstitial positions has two major effects on perovskite: 1) Deactivation of the deep trap levels leading to nonradiative recombination (interstitial bromide energy levels are shallower compared to interstitial iodide). 2) The substitution of interstitial iodide with bromide interstitial inhibits the photogenerated I_2 formation, obtaining more stable perovskite compositions.

3. Conclusion

In this work, we have investigated the defect chemistry of $FAPbI_3$ upon alloying with Br^-: the FA-based perovskite forms stable phases with perovskite compositions $(FAPbI_3)_{1-x}(FAPbBr_3)_x$ ranging from $X = 0$ to $X = 0.3$. Within this range, Br^- is homogenously incorporated as a solid solution with the iodide-based perovskite host and we did not observe evidence of phase segregation. After identifying the most stable perovskite compositions, we found that $X = 0.16$ and $X = 0.24$ result in higher PLQY values, with improvement in both spontaneous and amplified emission and better photostability leading to improved efficiency roll-off and higher radiance in LEDs. By employing photoemission electron microscopy we were able to directly probe the impact of Br^- alloying on the energetic landscape of the material correlating the improved performance to a reduced activity of hole trapping, which acts as a deep defect level causing detrimental nonradiative recombination of charge carriers. Importantly, the Br^-/I^- interstitial substitution can well explain the enhanced photostability of the material, for two possible concomitant reasons. In fact, it not only reduces the density of deep electronic defect states, but also removes those which can lead to material degradation, the interstitial iodide. The trapping of carriers at these defects results in neutral Ii^0 species (a coordinated I_2^- radical). The probability of forming I_2 moieties increases with the presence of the I_2^- radicals, via bimolecular processes (e.g., $2I_2^- \rightarrow I_2 + 2I^-$) or the capture of a second carrier (e.g., $I_2^- + 1h^+ \rightarrow I_2$). Finally, I_2 is released at the surface and at the grain boundaries, which triggers material degradation in pure-iodide perovskites. Such a process is less efficient when bromide is added given the higher probability of oxidation of the iodide site.[35] Our findings show that Br^- alloying in $FAPbI_3$ represents a valuable and synthetically straightforward strategy to control the defect chemistry of the material to harness the full potential of the material for both coherent and incoherent perovskite photonic platforms.

4. Experimental Section

Materials: Lead iodide (PbI_2, 99.99%), lead bromide ($PbBr_2$, 98%), 5-aminovaleric acid iodide (5-AVAI, 97%), and 5-aminovaleric acid bromide (5-AVABr, 98%), were purchased from Tokyo Chemical Industry (TCI). Formamidinium iodide (FAI) and formamidinium bromide (FABr) were purchased from Greatcell Solar Materials. Poly(9,9-dioctylfluorene-alt-*N*-(4-sec-butylphenyl)-diphenylamine) (TFB) was purchased from Ossila. *N*,*N*-Dimethylformamide (DMF, anhydrous 99.8%), dimethyl sulfoxide (DMSO, anhydrous 99.9%), chlorobenzene (CB, anhydrous 99.8%), m-xylene (anhydrous 99%), 2-methoxyethanol (99.9%), and polyethylenimine, 80% ethoxylated solution (PEIE, 37% in H_2O) were purchased from Sigma–Aldrich.

ZnO Nanoparticles Synthesis: ZnO nanoparticles (ZnO NPs) were synthesized following a solution-precipitation method. In short, 3 mmol of zinc acetate dihydrate ($Zn(CH_3COO)_2 \cdot 2H_2O$, 98% Sigma–Aldrich) were dissolved in 30 mL of DMSO (99% Sigma–Aldrich) at 30 °C. Then, 5.6 mmol of tetramethylammonium hydroxide pentahydrate ($((CH_3)_4N(OH) \cdot 5H_2O$, 95% Sigma–Aldrich) were dissolved in 10 mL of ethanol (anhydrous, 99.8% VWR), and were added dropwise to the zinc acetate solution and left it stirring at 30 °C for 24 h. Then, ZnO NPs were precipitated with ethyl acetate (anhydrous, 99.8% Sigma–Aldrich), washed with ethanol, and precipitated again with ethyl acetate. Then, the ZnO NPs were dispersed in ethanol. Finally, they were filtered using a 0.45 µm PTFE filter.

© 2023 The Authors. Advanced Functional Materials published by Wiley-VCH GmbH

16163028, 0, Downloaded from https://onlinelibrary.wiley.com/doi/10.1002/adfm.202308545 by Area Sistemi Dipart & Document, Wiley Online Library on [22/01/2024]. See the Terms and Conditions (https://onlinelibrary.wiley.com/terms-and-conditions) on Wiley Online Library for rules of use; OA articles are governed by the applicable Creative Commons License

Perovskite Precursor Solution Preparation: Perovskite precursor solutions $(FAPbI_3)_{1-x}(FAPbBr_3)_x$ with $x = 0$, 0.04, 0.08, 0.16, 0.24, 0.36, 0.5, 0.76, 1; and a final $[Pb^{2+}] = 0.15$ were prepared to mix different volume ratios of $FAPbI_3$ and $FAPbBr_3$ solutions ($1 - x$FAPbI$_3$:xFAPbBr$_3$, vol:vol), in both cases using a concentration of $[Pb^{2+}] = 0.15$ and a molar ratio FAX:PbX_2:5-AVAX (2.45:1:0.3) where X = I or Br, dissolved in DMF:DMSO (9:1, vol%).

Alternatively, $(FAPbI_3)_{1-x}(FAPbBr_3)_x$ with $x = 0.08$, 0.16, 0.24 were prepared using just $PbBr_2$ as the Br source. The final $[Pb^{2+}]$ was 0.15 M and the molar ratio FAI:PbI_2:$PbBr_2$:5-AVAI (2.45:1 − y:y:0.3; y = 0, 0.12, 0.24, 0.36) dissolved in DMF:DMSO (9:1, vol%).

All the solutions were left stirring overnight at room temperature prior to film fabrication.

Perovskite Film Fabrication: Glass substrates were ultrasonicated in water/Hellmanex solution, water, acetone, and IPA for 15 min each. They were dried with a strong N_2 flow, and treated with O_2/plasma for 10 min before the deposition of any layer. ZnO solution was spincoated at 4000 rpm for 40 s and annealed at 150 °C for 30 min. Then, the films were allowed to cool down before the deposition of the PEIE solution (3.9 mg/ml in 2-methoxyethanol) via spin-coating at 5000 rpm for 50 s. The films were annealed at 100 °C for 10 min and immediately transferred to a N_2-filled glove box. The perovskite layer was prepared by spin coating 80 µL of the perovskite precursor solution at 500 rpm for 3 s followed by a second step at 8000 rpm (or 2000 rpm to fabricate thicker samples for the ASE characterization) for 45 s. And 30 s before the end of the spinning process, 120 µL of chlorobenzene were spincoated on top of the spinning substrate. The substrates were annealed at 105 °C for 20 min.

For spectroscopic characterization, samples were encapsulated using a glass cover and a UV-curable epoxy resin to avoid the influence of oxygen and humidity.

Perovskite Light Emitting Diodes (PeLEDs) Fabrication: ITO substrates were etched with powder Zn and 2 M HCl. The etched films were cleaned with ultrasonication in water/Hellmanex solution, water, acetone, and IPA for 15 min each. The substrates were dried with a strong N_2-flow, and treated with O_2/plasma for 10 min before the deposition of any layer. ZnO NPs were spincoated at 4000 rpm for 40 s and annealed at 150 °C for 30 min. Substrates were allowed to cool down before the deposition of PEIE (3.9 mg/ml in 2-methoxyethanol) at 5000 rpm for 50 s, with the following annealing at 100 °C for 10 min. The substrates were immediately transferred to an N_2-filled glove box. The perovskite precursor solution was spincoated at 500 rpm for 3 s followed by 8000 rpm for 45 s. And 30 s before the end of the spin coating process, 120 µL of chlorobenzene was dropped on top of the spinning substrate. Then, TFB (10 mg/ml in m-xylene) was spincoated at 2000 rpm for 40 s. Finally, 10 nm of MoO_3 and 100 nm of Au were thermally evaporated at $\approx 10^{-6}$ mbar using a shadow mask to give a final active area of 0.1 cm^2.

Devices were encapsulated using a cover glass and a UV-curable epoxy resin to avoid the influence of humidity and oxygen.

PeLEDs used for the measurement of ASE under applied bias were optimized in order to promote the optoelectronic properties of the material and reduce optical losses at the electrode. For this reason, $[Pb^{2+}] = 0.5$ M solutions were employed while keeping the same molar ratio with the rest of the reagents. Also, a thicker layer of TFB was achieved by using 40 mg mL solutions in m-xylene. Both in the case of perovskite and TFB, the spin coating conditions were identical to the previous methods.

Morphological and Structural Characterization: Scanning electron microscopy (SEM) images were obtained using a MIRA3 TESCAN with an accelerating voltage of 5 kV. To avoid charging effects during the image acquisition, samples were prepared on top of ITO conductive glass.

X-ray diffraction (XRD) patterns of the samples were acquired using a Bruker D8 Advance diffractometer with Bragg–Brentano geometry equipped, with Cu Kα radiation ($\lambda = 1.544060$ Å), operating at 40 kV and 40 mA. The diffraction patterns were acquired at room temperature, with a step size of 0.04° and 1 s of acquisition time.

Film thickness was determined using a surface profiler Dektak 150 (Veeco).

Spectroscopic Characterization: Steady–state UV–vis absorption was measured on encapsulated samples fabricated on glass using a UV–vis–NIR spectrophotometer Lambda 1050 (Perkin Elmer).

Steady–state PL was measured using a CW 450 nm diode laser (Oxxius). Photoluminescence was collected on reflection mode at a right angle and focused on an optical fiber connected to an Ocean Optics Maya Pro 2000 spectrometer. Measurements were done at room temperature in air on encapsulated samples. PL stability measurements were acquired for a period of 30 s, or, alternatively, 10 min with spectrum acquired every minute. The PL stability plots were represented using the scientific color maps package.[36]

Absolute photoluminescence quantum yield (PLQY) was performed using an integrating sphere (Labsphere) and a CW 560 nm diode laser (Oxxius). The emitted light was collected with an Ocean Optics Maya Pro 2000 Spectrometer coupled with an optical fiber to the integrating sphere. The measurements were done on encapsulated samples in air at room temperature. PLQY values were calculated using the method described by DeMello et al.[60]

Fluence-dependent PLQY was acquired with a Yb:KGW laser (Light Conversion Pharos, 1030 nm) using the second harmonic (515 nm, 300 fs pulse duration, 500 kHz repetition rate) tightly focused on sample to achieve a fluence range between 0.275 and 300 µJ cm^{-2}, and collecting the emitted PL with an optical fiber coupled to a spectrometer (Ocean Optics Maya Pro 2000).

Micro-photoluminescence was acquired using a Nikon LV100ND upright commercial microscope, and a Nikon C-LHGFI mercury-vapor lamp as the excitation source. Optical and PL images were taken by a Nikon DS-Fi3 digital camera, while complete hyperspectral PL maps were measured by a Nireos HERA Vis–NIR—Hyperspectral Camera. The PL maps were represented by using the scientific colour map packages.[36]

Time-resolved photoluminescence (TRPL) using the second harmonic of Innolas Picolo (Ne:YVO_4, 532 nm, 1 kHz). The PL was detected with an Andor iStar 320T ICCD camera coupled to a Shamrock 303i spectrograph, using temporal step sizes from 5 to 100 ns and a fluence of 1.4 nJ cm^{-2}.

The ASE was characterized by measuring the photoluminescence at higher excitation densities. The films were excited with a Q-switched Nd:YVO_4 laser (Innolas Picolo, 1064 nm) using the second harmonic (532 nm, 900 ps pulse width, 1 kHz repetition rate). The beam was focused to a spot size of 870 µm, at quasi-normal incidence, and the resulting luminescence was collected with a fiber spectrometer (Ocean Optics Maya Pro 2000). All measurements were conducted on encapsulated samples. The ASE threshold was estimated from the fluence-dependent PL intensity, via the crossing of two linear fits close to the change of slope.

The ASE under a dc bias voltage was measured on an LED architecture, focusing the laser pump in the diode area. The laser setup conditions were identical to the measurement without an applied bias. The dc bias voltage was given using a Keithley 2401 source meter.

Photoemission electron microscopy (PEEM) and spectroscopy (PES): Before measurements, ≈30 nm thick sub-millimeter-sized gold markers were evaporated on all samples. The samples were then transferred from the glovebox to the microscope chamber using a nitrogen-filled container. All the measurements were carried out at room temperature in the ultrahigh vacuum chamber ($\approx 10^{-10}$ torr) of the microscope. The energy-resolved images and the spatial-resolved spectra were measured with 6 eV femtosecond pulses at 500 KHz repetition rate, with a field-of-view of 10 µm, and with the hemispherical energy analyzer set to an energy resolution of ≈ 250 meV. The photoemission spectra were referenced to the Fermi edge of nearby gold markers

Photothermal Deflection Spectroscopy (PDS): In the PDS, setup each sample was deposited on a quartz substrate and placed in a cuvette filled with a fluorinated liquid (tetradecafluorohexane) whose refractive index had a considerable temperature dependence.

The sample was then pumped with a laser beam selected by a SuperK SELECT acousto-optic tunable monochromator from a SuperK Extreme supercontinuum laser (NKT photonics) and then modulated at 4 Hz by a chopper to enable the lock-in detection; when the samples absorb it releases a part of the excitation by heat losses into the liquid generating a thermal lens (mirage effect). The probe laser (HeNe from JDSU), aligned

© 2023 The Authors. Advanced Functional Materials published by Wiley-VCH GmbH

16163028, 0, Downloaded from https://onlinelibrary.wiley.com/doi/10.1002/adfm.202308545 by Area Sistemi Dipart & Document, Wiley Online Library on [22/01/2024]. See the Terms and Conditions (https://onlinelibrary.wiley.com/terms-and-conditions) on Wiley Online Library for rules of use; OA articles are governed by the applicable Creative Commons License

closed and parallel to the sample surface was then deflected due to the change in refractive index of the liquid, and the amplitude of this deflection is measured by a quadrant detector (PDQ80A, Thorlabs). The deflection amplitude was linearly proportional to the absorbance of the sample so the absorption spectrum could be retrieved by varying the pump wavelength.[37]

The excitation laser beam passed through long-pass filters to prevent leakage of stray light and its intensity was measured by a photodiode to normalize the intensity of the deflection signal.

Device Characterization: Current–voltage (*I–V*) characteristics of the LED were acquired using a Keithley 2614B source meter in combination with a photodiode of known responsivity (OSI Optoelectronics, UV 100DQC). Measurements were done applying bias with a step voltage of 50 mV to the diode and the emitted light was collected by the photodiode placed at 10 cm from the device. The electroluminescence was registered with an Ocean Optics Maya 2000 Pro spectrometer. Device efficiencies were calculated assuming a Lambertian distribution of emission.

Supporting Information

Supporting Information is available from the Wiley Online Library or from the author.

Acknowledgements

This work was supported by the European Union's Horizon2020 research and innovation program under the ERC project SOPHY under grant agreement no. 771528, Marie Skłodowska-Curie Individual Fellowship under grant agreement no. 839480 (PERICLeS), MSCA-ITN PERSEPHONEunder grant agreement no. 956270 (PERSEPHONE), and MSCA-ITN SMART-X under grant agreement no. 860553. The authors thank Dr. H. Wang for useful discussions.

Conflict of Interest

The authors declare no conflict of interest.

Data Availability Statement

The data that support the findings of this study are available from the corresponding author upon reasonable request.

Keywords

carrier trapping, defects, halide mixing, light-emitting diodes, metal halide perovskite, photo-emission electron microscopy

Received: July 22, 2023
Revised: October 23, 2023
Published online:

[1] a) H. Min, D. Y. Lee, J. Kim, G. Kim, K. S. Lee, J. Kim, M. J. Paik, Y. K. Kim, K. S. Kim, M. G. Kim, T. J. Shin, S. I. Seok, *Nature* **2021**, *598*, 444; b) J. Park, J. Kim, H.-S. Yun, M. J. Paik, E. Noh, H. J. Mun, M. G. Kim, T. J. Shin, S. I. Seok, *Nature* **2023**, *616*, 724.

[2] a) Y. Cao, N. Wang, H. Tian, J. Guo, Y. Wei, H. Chen, Y. Miao, W. Zou, K. Pan, Y. He, H. Cao, Y. Ke, M. Xu, Y. Wang, M. Yang, K. Du, Z. Fu, D. Kong, D. Dai, Y. Jin, G. Li, H. Li, Q. Peng, J. Wang, W. Huang, *Nature* **2018**, *562*, 249; b) B. Guo, R. Lai, S. Jiang, L. Zhou, Z. Ren, Y. Lian, P. Li, X. Cao, S. Xing, Y. Wang, W. Li, C. Zou, M. Chen, Z. Hong, C. Li, B. Zhao, D. Di, *Nat. Photonics* **2022**, *16*, 637; c) Y. Sun, L. Ge, L. Dai, C. Cho, J. Ferrer Orri, K. Ji, S. J. Zelewski, Y. Liu, A. J. Mirabelli, Y. Zhang, J.-Y. Huang, Y. Wang, K. Gong, M. C. Lai, L. Zhang, D. Yang, J. Lin, E. M. Tennyson, C. Ducati, S. D. Stranks, L. S. Cui, N. C. Greenham, *Nature* **2023**, *615*, 830; d) W. Xu, Q. Hu, S. Bai, C. Bao, Y. Miao, Z. Yuan, T. Borzda, A. J. Barker, E. Tyukalova, Z. Hu, M. Kawecki, H. Wang, Z. Yan, X. Liu, X. Shi, K. Uvdal, M. Fahlman, W. Zhang, M. Duchamp, J. M. Liu, A. Petrozza, J. Wang, L.-M. Liu, W. Huang, F. Gao, *Nat. Photonics* **2019**, *13*, 418.

[3] a) W. B. Gunnarsson, B. P. Rand, *APL Mater.* **2020**, *8*, 030902; b) L. Lei, Q. Dong, K. Gundogdu, F. So, *Adv. Funct. Mater.* **2021**, *31*, 2010144; c) A. Liu, G. Guan, X. Chai, N. Feng, M. Lu, X. Bai, Y. Zhang, *Laser Photonics Rev.* **2022**, *16*, 2200189.

[4] a) S. D. Stranks, S. M. Wood, K. Wojciechowski, F. Deschler, M. Saliba, H. Khandelwal, J. B. Patel, S. J. Elston, L. M. Herz, M. B. Johnston, A. P. H. J. Schenning, M. G. Debije, M. K. Riede, S. M. Morris, H. J. Snaith, *Nano Lett.* **2015**, *15*, 4935; b) G. Xing, N. Mathews, S. S. Lim, N. Yantara, X. Liu, D. Sabba, M. Grätzel, S. Mhaisalkar, T. C. Sum, *Nat. Mater.* **2014**, *13*, 476; c) X. Zeng, Z. Liu, H. Du, Z. Wang, M. Li, M. Pi, J. Tan, D. Zhang, J. Yang, J. Du, *Adv. Opt. Mater.* **2022**, *10*, 2201328.

[5] a) X. Gao, J. Lin, X. Guo, G. He, D. Zou, T. Ishii, D. Zhang, C. Zhao, H. Zhan, J. S. Huang, X. Liu, C. Adachi, C. Qin, L. Wang, *J. Phys. Chem. Lett.* **2023**, *14*, 2493; b) L. Lei, D. Seyitliyev, S. Stuard, J. Mendes, Q. Dong, X. Fu, Y.-A. Chen, S. He, X. Yi, L. Zhu, C. H. Chang, H. Ade, K. Gundogdu, F. So, *Adv. Mater.* **2020**, *32*, 1906571; c) C. Qin, A. S. D. Sandanayaka, C. Zhao, T. Matsushima, D. Zhang, T. Fujihara, C. Adachi, *Nature* **2020**, *585*, 53.

[6] a) A. Binek, F. C. Hanusch, P. Docampo, T. Bein, *J. Phys. Chem. Lett.* **2015**, *6*, 1249; b) T. Chen, B. J. Foley, C. Park, C. M. Brown, L. W. Harriger, J. Lee, J. Ruff, M. Yoon, J. J. Choi, S. H. Lee, *Sci. Adv.* **2016**, *2*, e1601650; c) C. C. Stoumpos, C. D. Malliakas, M. G. Kanatzidis, *Inorg. Chem.* **2013**, *52*, 9019.

[7] Y. H. Jia, S. Neutzner, Y. Zhou, M. Yang, J. M. F. Tapia, N. Li, H. Yu, J. Cao, J. P. Wang, A. Petrozza, C. P. Wong, N. Zhao, *Adv. Funct. Mater.* **2020**, *30*, 1906875.

[8] a) D. Meggiolaro, S. G. Motti, E. Mosconi, A. J. Barker, J. Ball, C. Andrea Riccardo Perini, F. Deschler, A. Petrozza, F. De Angelis, *Energy Environ. Sci.* **2018**, *11*, 702; b) S. G. Motti, D. Meggiolaro, S. Martani, R. Sorrentino, A. J. Barker, F. De Angelis, A. Petrozza, *Adv. Mater.* **2019**, *31*, 1901183; c) Y. Zhou, I. Poli, D. Meggiolaro, F. De Angelis, A. Petrozza, *Nat. Rev. Mater.* **2021**, *6*, 986.

[9] a) S. Feldmann, S. Macpherson, S. P. Senanayak, M. Abdi-Jalebi, J. P. H. Rivett, G. Nan, G. D. Tainter, T. A. S. Doherty, K. Frohna, E. Ringe, R. H. Friend, H. Sirringhaus, M. Saliba, D. Beljonne, S. D. Stranks, F. Deschler, *Nat. Photonics* **2020**, *14*, 123; b) K. Frohna, M. Anaya, S. Macpherson, J. Sung, T. A. S. Doherty, Y.-H. Chiang, A. J. Winchester, K. W. P. Orr, J. E. Parker, P. D. Quinn, K. M. Dani, A. Rao, S. D. Stranks, *Nat. Nanotechnol.* **2022**, *17*, 190.

[10] a) A. Johnston, G. Walters, M. I. Saidaminov, Z. Huang, K. Bertens, N. Jalarvo, E. H. Sargent, *ACS Nano* **2020**, *14*, 15107; b) X. Zhao, H. Lu, W. H. Fang, R. Long, *Nanoscale* **2022**, *14*, 4644.

[11] D. P. Mcmeekin, G. Sadoughi, W. Rehman, G. E. Eperon, M. Saliba, M. T. Hörantner, A. Haghighirad, N. Sakai, L. Korte, B. Rech, M. B. Johnston, L. M. Herz, H. J. Snaith, *Science* **2016**, *351*, 151.

[12] T. Ungár, *Scripta Mater.* **2004**, *51*, 777.

[13] a) Y. Chen, S. G. Motti, R. D. J. Oliver, A. D. Wright, H. J. Snaith, M. B. Johnston, L. M. Herz, M. R. Filip, *J. Phys. Chem. Lett.* **2022**, *13*, 4184; b) M. Kato, T. Fujiseki, T. Miyadera, T. Sugita, S. Fujimoto, M. Tamakoshi, M. Chikamatsu, H. Fujiwara, *J. Appl. Phys.* **2017**, *121*, 115501.

© 2023 The Authors. Advanced Functional Materials published by Wiley-VCH GmbH

16163028, 0, Downloaded from https://onlinelibrary.wiley.com/doi/10.1002/adfm.202308545 by Area Sistemi Dipart & Document, Wiley Online Library on [22/01/2024]. See the Terms and Conditions (https://onlinelibrary.wiley.com/terms-and-conditions) on Wiley Online Library for rules of use; OA articles are governed by the applicable Creative Commons License

[14] a) S. De Wolf, J. Holovsky, S. J. Moon, P. Löper, B. Niesen, M. Ledinsky, F. J. Haug, J.-H. Yum, C. Ballif, *J. Phys. Chem. Lett.* **2014**, *5*, 1035; b) A. Sadhanala, F. Deschler, T. H. Thomas, S. E. Dutton, K. C. Goedel, F. C. Hanusch, M. L. Lai, U. Steiner, T. Bein, P. Docampo, D. Cahen, R. H. Friend, *J. Phys. Chem. Lett.* **2014**, *5*, 2501.
[15] Y. Yang, M. Yang, Z. Li, R. Crisp, K. Zhu, M. C. Beard, *J. Phys. Chem. Lett.* **2015**, *6*, 4688.
[16] a) M. C. Brennan, A. Ruth, P. V. Kamat, M. Kuno, *Trends Chem.* **2020**, *2*, 282; b) A. Ruth, H. Okrepka, P. Kamat, M. Kuno, *J. Phys. Chem. C* **2023**, *127*, 18547.
[17] Y. Li, Y. Lu, X. Huo, D. Wei, J. Meng, J. Dong, B. Qiao, S. Zhao, Z. Xu, D. Song, *RSC Adv.* **2021**, *11*, 15688.
[18] M. Long, T. Zhang, M. Liu, Z. Chen, C. Wang, W. Xie, F. Xie, J. Chen, G. Li, J. Xu, *Adv. Mater.* **2018**, *30*, 1801562.
[19] V. Diez-Cabanes, J. Even, D. Beljonne, C. Quarti, *Adv. Opt. Mater.* **2021**, *9*, 2001832.
[20] W. Rehman, R. L. Milot, G. E. Eperon, C. Wehrenfennig, J. L. Boland, H. J. Snaith, M. B. Johnston, L. M. Herz, *Adv. Mater.* **2015**, *27*, 7938.
[21] E. T. Hoke, D. J. Slotcavage, E. R. Dohner, A. R. Bowring, H. I. Karunadasa, M. D. Mcgehee, *Chem. Sci.* **2015**, *6*, 613.
[22] Y. Zhou, Y. H. Jia, H. H. Fang, M. A. Loi, F. Y. Xie, L. Gong, M. C. Qin, X. H. Lu, C. P. Wong, N. Zhao, *Adv. Funct. Mater.* **2018**, *28*, 1803130.
[23] a) M. B. Johnston, L. M. Herz, *Acc. Chem. Res.* **2016**, *49*, 146; b) S. D. Stranks, V. M. Burlakov, T. Leijtens, J. M. Ball, A. Goriely, H. J. Snaith, *Phys. Rev. Appl.* **2014**, *2*, 034007.
[24] Z. Yuan, Y. Miao, Z. Hu, W. Xu, C. Kuang, K. Pan, P. Liu, J. Lai, B. Sun, J. Wang, S. Bai, F. Gao, *Nat. Commun.* **2019**, *10*, 2818.
[25] C. Kuang, Z. Hu, Z. Yuan, K. Wen, J. Qing, L. Kobera, S. Abbrent, J. Brus, C. Yin, H. Wang, W. Xu, J. Wang, S. Bai, F. Gao, *Joule* **2021**, *5*, 618.
[26] M. Yang, N. Wang, S. Zhang, W. Zou, Y. He, Y. Wei, M. Xu, J. Wang, W. Huang, *J. Phys. Chem. Lett.* **2018**, *9*, 2038.
[27] a) C. Zou, Y. Liu, D. S. Ginger, L. Y. Lin, *ACS Nano* **2020**, *14*, 6076; b) W. Zou, R. Li, S. Zhang, Y. Liu, N. Wang, Y. Cao, Y. Miao, M. Xu, Q. Guo, D. Di, L. Zhang, C. Yi, F. Gao, R. H. Friend, J. Wang, W. Huang, *Nat. Commun.* **2018**, *9*, 608.
[28] A. Fakharuddin, W. Qiu, G. Croes, A. Devizis, R. Gegevicius, A. Vakhnin, C. Rolin, J. Genoe, R. Gehlhaar, A. Kadashchuk, V. Gulbinas, P. Heremans, *Adv. Funct. Mater.* **2019**, *29*, 1904101.
[29] L. Zhao, K. Roh, S. Kacmoli, K. Al Kurdi, S. Jhulki, S. Barlow, S. R. Marder, C. Gmachl, B. P. Rand, *Adv. Mater.* **2020**, *32*, 2000752.
[30] a) Y. Guo, S. Apergi, N. Li, M. Chen, C. Yin, Z. Yuan, F. Gao, F. Xie, G. Brocks, S. Tao, N. Zhao, *Nat. Commun.* **2021**, *12*, 644; b) Y. Jia, H. Yu, Y. Zhou, N. Li, Y. Guo, F. Xie, Z. Qin, X. Lu, N. Zhao, *ACS Appl. Mater. Interfaces* **2021**, *13*, 28546; c) H. Zhang, C. Tu, C. Xue, J. Wu, Y. Cao, W. Zou, W. Xu, K. Wen, J. Zhang, Y. Chen, J. Lai, L. Zhu, K. Pan, L. Xu, Y. Wei, H. Lin, N. Wang, W. Huang, J. Wang, *Nano Lett.* **2021**, *21*, 3738.
[31] a) Y. Li, H. Hu, A. Farag, T. Feeney, I. Allegro, U. Lemmer, U. W. Paetzold, I. A. Howard, *Nano Lett.* **2023**, *23*, 1637; b) P. Liu, C. Gu, Q. Liao, *ACS Omega* **2021**, *6*, 34021.
[32] G. Mei, D. Wu, S. Ding, W. C. H. Choy, K. Wang, X. W. Sun, *IEEE Photonics J* **2020**, *12*, 1.
[33] H. Wang, Z. Chen, J. Hu, H. Yu, C. Kuang, J. Qin, X. Liu, Y. Lu, M. Fahlman, L. Hou, X.-K. Liu, F. Gao, *Adv. Funct. Mater.* **2021**, *31*, 2007596.
[34] a) T. A. S. Doherty, A. J. Winchester, S. Macpherson, D. N. Johnstone, V. Pareek, E. M. Tennyson, S. Kosar, F. U. Kosasih, M. Anaya, M. Abdi-Jalebi, Z. Andaji-Garmaroudi, E. L. Wong, J. Madéo, Y.-H. Chiang, J.-S. Park, Y. K. Jung, C. E. Petoukhoff, G. Divitini, M. K. L. Man, C. Ducati, A. Walsh, P. A. Midgley, K. M. Dani, S. D. Stranks, *Nature* **2020**, *580*, 360; b) S. Kosar, A. J. Winchester, T. A. S. Doherty, S. Macpherson, C. E. Petoukhoff, K. Frohna, M. Anaya, N. S. Chan, J. Madéo, M. K. L. Man, S. D. Stranks, K. M. Dani, *Energy Environ. Sci.* **2021**, *14*, 6320; c) S. Macpherson, T. A. S. Doherty, A. J. Winchester, S. Kosar, D. N. Johnstone, Y.-H. Chiang, K. Galkowski, M. Anaya, K. Frohna, A. N. Iqbal, S. Nagane, B. Roose, Z. Andaji-Garmaroudi, K. W. P. Orr, J. E. Parker, P. A. Midgley, K. M. Dani, S. D. Stranks, *Nature* **2022**, *607*, 294.
[35] a) S. Martani, Y. Zhou, I. Poli, E. Aktas, D. Meggiolaro, J. Jiménez-López, E. L. Wong, L. Gregori, M. Prato, D. Di Girolamo, A. Abate, F. De Angelis, A. Petrozza, *ACS Energy Lett.* **2023**, *8*, 2801; b) G. F. Samu, Á. Balog, F. De Angelis, D. Meggiolaro, P. V. Kamat, C. Janáky, *J. Am. Chem. Soc.* **2019**, *141*, 10812.
[36] F. Crameri, in *Scientific Colour Maps*, Zenodo, France **2023**.
[37] W. B. Jackson, N. M. Amer, A. C. Boccara, D. Fournier, *Appl. Opt.* **1981**, *20*, 1333.

© 2023 The Authors. Advanced Functional Materials published by Wiley-VCH GmbH

16163028, 0, Downloaded from https://onlinelibrary.wiley.com/doi/10.1002/adfm.202308545 by Area Sistemi Dipart & Document, Wiley Online Library on [22/01/2024]. See the Terms and Conditions (https://onlinelibrary.wiley.com/terms-and-conditions) on Wiley Online Library for rules of use; OA articles are governed by the applicable Creative Commons License